Chapter 3
Monte Carlo Transport Calculation

This chapter is devoted to the description of a single particle Monte Carlo method and an ensemble Monte Carlo method. The description uses flowcharts followed by appropriate FORTRAN codes so that the reader can develop his or her own Monte Carlo program. The FORTRAN codes presented in this chapter are only appropriate for the carrier transport in spherical and parabolic bands. Although this may not be a reasonable approximation for some commonly used semiconductors, this choice allows one to present simple programs that are easy to understand. The description is supplemented by topics on carrier transport in ellipsoidal and non-parabolic bands to provide the reader with a more complete description. Hence, it probably will not be difficult for readers to modify sample programs for their own purposes. Some practical programs for bulk silicon and GaAs are presented in Appendix 6. The topics given in this chapter may also provide a good basis for the self-consistent ensemble Monte Carlo method used for device simulation.

3.1 SINGLE-PARTICLE MONTE CARLO

The analysis of the carrier transport in a semiconductor is a many-body problem with a large number of carriers mutually interacting; hence, it is a very difficult task. However, when the many-body system can be considered an ensemble of independent carriers, it becomes possible to use an approximate method that simulates the ensemble of carriers by monitoring the history of a single carrier undergoing many scattering events. This is the principal idea of the single particle Monte Carlo technique.

The single-particle Monte Carlo method has been used for calculating transport properties of carriers in homogeneous bulk semiconductors [1–3]. It is straightforward and can be carried out without the need of assuming the shape of the

distribution function. It is also very useful to calculate ensemble relaxation rates (or times), which are applied for the balance equation method explained in Chapter 5. The method is easy to learn and the program for simulation is also easy to develop.

3.1.1 Simulation of Carrier Motion

The principle of the single-particle Monte Carlo method applied to the transport analysis is to simulate the motion of a single carrier in the momentum space. This is done by selecting the duration of the carrier free flights and the scattering events stochastically. The simulation is therefore made by generating a sequence of random numbers. The simulation program can be constructed by preparing a couple of subroutines simulating the drift and scattering processes. If the subroutines for drift and scattering processes are denoted by **drift** and **scat**, respectively, then the simulation process is described by a simple flowchart shown in Figure 3.1. The details of the **drift** and **scat** subroutines are explained in the following sections.

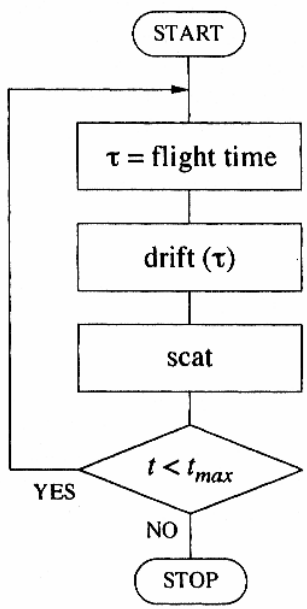

Figure 3.1 Flowchart of the single-particle Monte Carlo calculation.

The simulation process repeatedly evaluates the drift motion under a constant electric field followed by scattering due to impurities, phonons, and so on. As shown in Figure 3.1, these two subroutines are executed alternately, and the *duration of free flight* (or the *flight time*) is determined in each iteration.

The duration of free flight depends on the total scattering rate which is the sum of various scattering rates. Since the scattering rate for each scattering mechanism is a function of electron energy, the total scattering rate is also a function of electron energy. The probability per unit time, $P(\tau)$, of an electron traveling for a time τ and then being scattered at the end of this flight, is given by

$$P(\tau) = W_T(E_k) \exp\left[-\int_0^\tau W_T(E_k)dt\right] \tag{3.1}$$

where $W_T(E_k)$ is the total scattering rate given by

$$W_T(E_k) = \sum_{j=1}^{N} W_j(E_k) \tag{3.2}$$

Here the subscript j denotes a scattering mechanism and takes the values $j = 1, 2, \ldots, N$ for N possible scattering mechanisms. To determine the flight time by making use of (3.1), we have to evaluate τ for a given $P(\tau)/W_T(E_k)$ specified by a random number r_1 distributed uniformly between 0 and 1. However, the integral can not be evaluated analytically because of the complicated form of each $W_j(E_k)$, as shown in Chapter 2.

A simple alternative technique for overcoming the difficulty in evaluating the integral of (3.1) has been developed by introducing a virtual scattering process (called *self-scattering* in the following) that makes no change to the **k** vector of the particle and whose scattering rate, $W_0(E_k)$, is so chosen that the new total scattering rate Γ becomes constant [2]; thus,

$$W_0(E_k) = \Gamma - \sum_{j=1}^{N} W_j(E_k) \quad \text{or} \quad \Gamma = \sum_{j=0}^{N} W_j(E_k) \tag{3.3}$$

This approach has an advantage because (3.1) can be written simply as

$$P(\tau) = \Gamma e^{-\Gamma\tau} \tag{3.4}$$

The flight time can be consequently determined by substituting a uniform random number r_1 into the following analytical form:

$$\tau = -\frac{\ln(r_1)}{\Gamma} \tag{3.5}$$

The constant Γ is taken to be larger than the largest value of $W_T(E_k)$ to avoid a negative value of $W_0(E_k)$ within the energy range of interest. A smaller Γ is, however, desirable to minimize the number of self-scattering events. Having determined the time of free flight, it is possible to calculate the drift process based on the equation of motion, as described in Section 3.1.2.

An example of FORTRAN code of a subroutine named **smc** to perform the single-particle Monte Carlo is shown in Figure 3.2, and the description of the parameters used in **smc** is given in Table 3.1. The function **rnd()** generates uniform random numbers distributed between 0 and 1. Line 12 in Figure 3.2 indicates the calculation of the flight time as given by (3.5). After the free flight, the electron

```
 1 c
 2 c===( A routine for single )===
 3 c===( particle Monte Carlo )===
 4 c
 5       subroutine smc
 6       common
 7      &/gamma/gm
 8      &/time/tmax
 9 c
10       t=0.
11 c
12    10 tau = - alog(rnd())/gm
13       call drift(tau)
14       call scat
15       t    = t + tau
16       if (t.lt.tmax) goto 10
17 c
18       return
19       end
```

Figure 3.2 FORTRAN code of **smc** to perform the single particle Monte Carlo calculation.

Table 3.1
Parameters Used in the Subroutine **smc**

Parameter	*Description*
t	Time variable
tau	Flight time, τ, in (3.5)
rnd()	Random number generator
gm	Total scattering rate including self-scattering, Γ, in (3.3)
tmax	Simulation time

will be scattered again by one of the scattering mechanisms, including self-scattering. In the scattering calculation, we have to identify first the scattering mechanism by which the electron is to be scattered and then determine the electron state after scattering. These topics are discussed in Section 3.1.3.

The simulation is started by choosing an arbitrary wave vector as the initial condition of the particle, and is allowed to proceed until many flight and scattering events have occurred. The total flight time (the sum of each flight time) must be long enough so that the initial condition has little influence on the final results. As the simulation time goes on, the results become more precise. However, we need a compromise to save computer time.

3.1.2 Drift Process

As discussed in Chapter 1, the drift motion of electrons in a semiconductor crystal can be treated semi-classically if the potential energy for the electron varies slowly as a function of position, and thus electrons can be regarded as free particles with an effective mass. Based on the equations of motion for electrons presented in Chapter 1, the change in the wave vector during the flight time τ is obtained by integrating the equation of motion (1.16a) with respect to time; thus,

$$\Delta\mathbf{k} = -\frac{1}{\hbar}\int_t^{t+\tau} \nabla H \, dt' \tag{3.6}$$

where H is the total energy (or Hamiltonian) of an electron with a charge $-e$ given by

$$H = E_k - eV(\mathbf{r}) \tag{3.7}$$

and where E_k is the kinetic energy of the electron and $V(\mathbf{r})$ is the electrostatic

potential. If a uniform electric field **F** is applied across a bulk semiconductor, (3.6) has a solution,

$$\Delta \mathbf{k} = -\frac{e\mathbf{F}}{\hbar}\tau \tag{3.8}$$

A FORTRAN code for the subroutine **drift**, which is based on (3.8), is shown in Figure 3.3, where we assumed that only the x-component of the electric field is non-zero. The subroutine **drift** is written for bulk GaAs to illustrate the case of a multivalley semiconductor. A simple two-valley model is employed, in which only the Γ- and L-valleys are taken into account. Both Γ- and L-valleys are assumed to be spherical and parabolic. The parameters used in the subroutine are described in Table 3.2. Line 11 in the list shown in Figure 3.3 calculates the increment of **k** according to (3.8). The wave vector **k** updated by the subroutine **drift** is transferred to the subroutine **scat**, via the common block named */com1/*, and is used as the initial state of the scattering. The scattering calculation is described in the next section.

3.1.3 Scattering Process

In the scattering calculation made by the subroutine **scat**, we select first a scattering mechanism by which an electron is to be scattered, and then identify the electron state after the scattering. The selection of a scattering mechanism (n) can be made by using functions $\Lambda_n(E_\mathbf{k})$ defined as

$$\Lambda_n(E_\mathbf{k}) = \frac{\sum_{j=1}^{n} W_j(E_\mathbf{k})}{\Gamma} \qquad \text{for } n = 1, 2, \ldots, N \tag{3.9}$$

which are the successive summations of the scattering rates normalized with Γ. Γ is identical to the parameter defined by (3.3), and N is the total number of scattering mechanisms. A scattering mechanism for an electron with energy $E_\mathbf{k}$ is selected by generating a random number r_2 lying between 0 and 1, and comparing it to $\Lambda_n(E_\mathbf{k})$; thus, the n-th scattering mechanism is chosen if the condition given by

$$\Lambda_{n-1}(E_\mathbf{k}) < r_2 \le \Lambda_n(E_\mathbf{k}) \qquad n = 1, 2, \ldots, N \tag{3.10}$$

is satisfied. The selection of a scattering mechanism made by (3.10) implies that Pauli's exclusion principle is not taken into account, because the carrier occupancy in the final states is ignored. This is an assumption used throughout the Monte


```
 1 c
 2 c===( Calculation of drift process )===
 3 c
 4        subroutine drift(tau)
 5        common
 6       &/com1/kx,ky,kz,iv
 7       &/dri/qh
 8       &/field/fx
 9        real kx,ky,kz
10 c
11        dkx = qh*fx*tau
12        kx  = kx+dkx
13 c
14        return
15        end
```

Figure 3.3 FORTRAN code for the subroutine **drift**.

Table 3.2
Parameters Used in the Subroutine **drift**

Parameter	*Description*
kx, ky, kz	Components of wave vector
iv	Valley index { iv = 1 for Γ-valley; iv = 2 for L-valley }
qh	$e/\hbar$
fx	Electric field (only x-component)
tau	Flight time

Carlo simulations described in this book, although some attempts have been made to include Pauli's exclusion principle [3].

Figure 3.4 shows schematically how a scattering mechanism $W_4(E_\mathbf{k})$ is chosen with the use of $\Lambda_n(E_\mathbf{k})$ and a random number r_2. The method of the selection is also described by the flowchart shown in Figure 3.5. Since the calculation of $W_j(E_\mathbf{k})$ (or $\Lambda_n(E_\mathbf{k})$) for a given $E_\mathbf{k}$ is time-consuming, it is desirable to prepare $\Lambda_n(E_\mathbf{k})$ tabular form for discrete values of $E_\mathbf{k}$ in an actual coding of the subroutine **scat**.

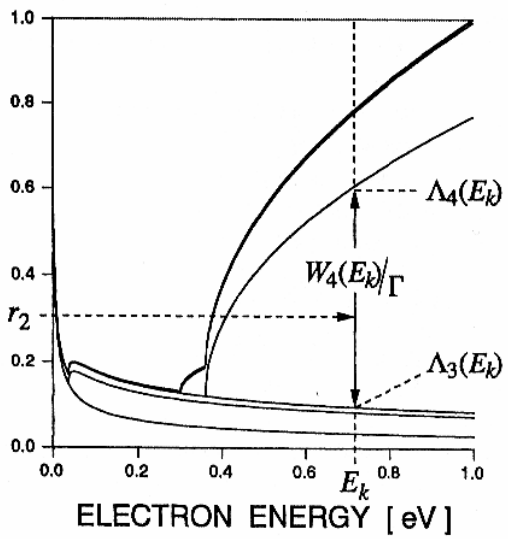

Figure 3.4 Schematic diagram showing the selection of a scattering mechanism by making use of $\Lambda_n(E_k)$. $W_4(E_k)$ is chosen by a random number r_2.

Figure 3.6 shows the first half of a FORTRAN code of **scat**, in which the selection of a scattering mechanism is made. The subroutine **scat** shown in this example is also written for bulk GaAs to be consistent with the subroutine **drift** described in Section 3.1.2. The parameters used in the subroutine are summarized in Table 3.3. The scattering mechanisms taken into account are the intra- and inter-valley phonon scatterings and the ionized impurity scattering. As explained before, $\Lambda_n(E_k)$ must be calculated in tabular form in advance by some other subroutine and saved in the dimension *swk*(*iv*, *n*, *ie*), where *iv* is the valley index, *n* denotes the *n*-th scattering mechanism, and *ie* is an integer proportional to the discretized particle energy. The reader is encouraged to do an exercise by rewriting the subroutine for a three-valley model (a model taking into account Γ-, L-, and X-valleys) by assigning a new integer value for the valley index *iv*.

Having determined the scattering mechanism, we next determine the wave vector $\mathbf{k}'$ after scattering. The magnitude of $\mathbf{k}'$ is known by the energy conservation. The direction of $\mathbf{k}'$ needs to be determined in terms of its components in a Cartesian coordinate (k_x^L, k_y^L, k_z^L) according to the *laboratory frame* (x^L, y^L, z^L) chosen for the simulated device.

If the scattering is isotropic (i.e., if the scattered electron has the same prob-

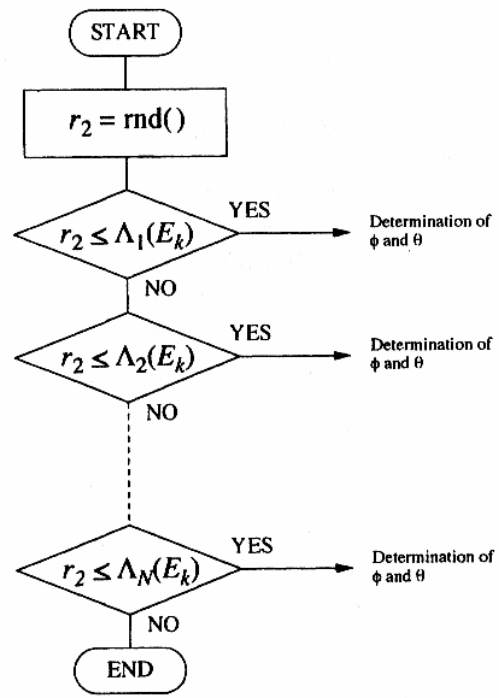

Figure 3.5 Flowchart for the selection of a scattering mechanism.

ability of being in any direction after scattering), the components k_x', k_y', and k_z' can be found by considering that the probability density $p(\phi', \theta')d\phi' d\theta'$ is proportional to the number of available states on a sphere of radius k', where ϕ' and θ' are the azimuthal and polar angles of $\mathbf{k}'$ with respect to k_z^L. $p(\phi', \theta')$ equals $\sin\theta'$, since any ϕ' is equally probable. Therefore, ϕ' and θ' can be determined by a couple of uniform random numbers, r_3 and r_4, lying between 0 and 1.

$$\begin{aligned} \phi' &= 2\pi r_3 \\ \cos\theta' &= 1 - 2r_4 \end{aligned} \tag{3.11}$$

For ϕ' and θ' given by (3.11), the components of the laboratory frame (k_x^L, k_y^L, k_z^L) are readily obtained as

```
c
c===( Calculation of scattering process )===
c
      subroutine scat
      common
     &/rate/hwo,hwij,hwe,de,swk(2,8,1000)
     &/com1/kx,ky,kz,iv
     &/ek/smh(2),hhm(2),ec(2)
     &/imp2/qd2
     &/emax/iemax
      real kx,ky,kz,ki,kf
c
      parameter( pi=3.14159 )
c
      skx = kx*kx
      sky = ky*ky
      sk  = skx+sky+kz*kz
      if (sk.eq.0.) return
c
      ei  = hhm(iv)*sk
      ie  = min(ifix(ei/de)+1,iemax)
      ki  = sqrt(sk)
      r1  = rnd()
c
      go to (1000,2000),iv
      return
```

Figure 3.6 First half of FORTRAN code for the subroutine **scat**.

$$
\begin{aligned}
k'_x &= k' \sin\theta' \cos\phi' \\
k'_y &= k' \sin\theta' \sin\phi' \\
k'_z &= k' \cos\theta'
\end{aligned}
\tag{3.12}
$$

These expressions are only valid for the case of isotropic scattering.

For anisotropic scattering processes, such as impurity scattering and polar optical phonon scattering, the final state $\mathbf{k}'$ is denoted by θ and ϕ, which are the


```
c---( Selection of scattering process )---
c---( in Gamma valley                 )---
c
 1000 if (r1.le.swk(iv,1,ie)) then
         ef=ei-hwo
         if (ef.le.0.) return
         go to 20
      elseif (r1.le.swk(iv,2,ie)) then
         ef=ei+hwo
         go to 20
      elseif (r1.le.swk(iv,3,ie)) then
         ef=ei
         r2=rnd()
         cb=1.-2.*r2/(1.+(1.-r2)*4.*sk/qd2)
         kf=ki
         go to 30
      elseif (r1.le.swk(iv,4,ie)) then
         ef=ei-hwij+ec(1)-ec(2)
         if (ef.le.0.) return
         iv=2
         go to 40
      elseif (r1.le.swk(iv,5,ie)) then
         ef=ei+hwij+ec(1)-ec(2)
         iv=2
         go to 40
      elseif (r1.le.swk(iv,6,ie)) then
         ef=ei
         go to 40
      endif
      return
```

Figure 3.6 Continued

polar and azimuthal angles of $\mathbf{k}'$ with respect to the initial wave vector $\mathbf{k}$. As before, we again have to express $\mathbf{k}'$ in terms of the components k'_x, k'_y, and k'_z in the chosen laboratory frame.

```
c---( Selection of scattering process )---
c---( in L valleys                    )---
c
 2000 if (rl.le.swk(iv,1,ie)) then
         ef=ei-hwo
         if (ef.le.0.) return
         go to 20
      elseif (rl.le.swk(iv,2,ie)) then
         ef=ei+hwo
         go to 20
      elseif (rl.le.swk(iv,3,ie)) then
         ef=ei
         r2=rnd()
         cb=1.-2.*r2/(1.+(1.-r2)*4.*sk/qd2)
         kf=ki
         go to 30
      elseif (rl.le.swk(iv,4,ie)) then
         ef=ei-hwe
         go to 40
      elseif (rl.le.swk(iv,5,ie)) then
         ef=ei+hwe
         go to 40
      elseif (rl.le.swk(iv,6,ie)) then
         ef=ei-hwij+ec(2)-ec(1)
         if (ef.le.0.) return
         iv=1
         go to 40
      elseif (rl.le.swk(iv,7,ie)) then
         ef=ei+hwij+ec(2)-ec(1)
         iv=1
         go to 40
```

Figure 3.6 Continued


```
      elseif (rl.le.swk(iv,8,ie)) then
         ef=ei
         go to 40
      endif
      return
```

Figure 3.6 Continued

Table 3.3
Parameters Used in the Subroutine scat

Parameter	*Description*
kx, ky, kz	Electron wave vector, k_x, k_y, and k_z
iv	Valley index
hwo, hwij, hwe	Phonon energy, $\hbar\omega_0$, $\hbar\omega_{ij}$, and $\hbar\omega_e$
de	Energy increment, E_k = de x ie
swk(iv, n, ie)	$\Lambda_n(E_k)$ in (3.9)
iemax	$E_{k\,\max}$ = de x iemax
smh(iv)	$\begin{cases}\sqrt{2m_t^* e}/\hbar \text{ for iv} = 1\\ \sqrt{2m_L^* e}/\hbar \text{ for iv} = 2\end{cases}$
hhm(iv)	$\begin{cases}\hbar^2/2m_t^* e \text{ for iv} = 1\\ \hbar^2/2m_L^* e \text{ for iv} = 2\end{cases}$
ec(iv)	Energy minima of valley iv
qd2	q_D^2 in (2.38)

The azimuthal angle ϕ can also be determined randomly because the transition rate is independent of ϕ, as discussed in Chapter 2; thus, ϕ can be found from

$$\phi = 2\pi r_3 \tag{3.13}$$

where r_3 is a uniform random number lying between 0 and 1.

For the impurity scattering and the polar optical phonon scattering, the polar angle θ are given, respectively, by (2.54) and (2.106). These formulas are repeated here:

$$\cos\theta = 1 - \frac{2r_4}{1 + (1 - r_4)\left(\dfrac{2k}{q_D}\right)^2} \tag{3.14}$$

for impurity scattering, and

$$\cos\theta = \frac{1 + f - (1 + 2f)^{r_s}}{f}$$
$$f = \frac{2\sqrt{E_{\mathbf{k}}E_{\mathbf{k}'}}}{(\sqrt{E_{\mathbf{k}}} - \sqrt{E_{\mathbf{k}'}})^2} \tag{3.15}$$

for polar optical phonon scattering.

We next discuss how the components of $\mathbf{k}'$ can be derived in the laboratory frame for the case of anisotropic scattering, such as impurity and polar optical phonon scattering. The azimuthal angle ϕ is given by (3.13) and the polar angle is given by either (3.14) or (3.15). When updating the orientation of the electron wave vector $\mathbf{k}$ in a laboratory frame (k_x^L, k_y^L, k_z^L), it is convenient to work with a new frame (k_x^r, k_y^r, k_z^r), in which the k_z-axis is parallel to the initial wave vector $\mathbf{k}$. The new frame is obtained by rotating (k_x^L, k_y^L, k_z^L) by an angle α about the k_x-axis and then β about the k_z-axis, as illustrated in Figure 3.7; hence, we need

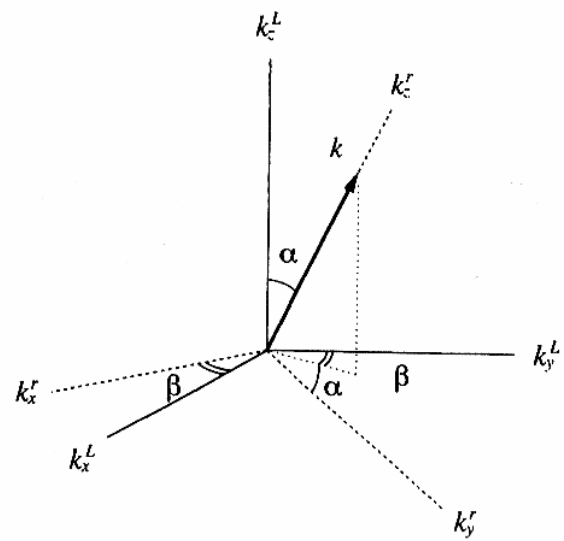

Figure 3.7 Relation between the laboratory frame (k_x^L, k_y^L, k_z^L) and a new frame (k_x^r, k_y^r, k_z^r), in which the k_z-axis is parallel to the initial wave vector $\mathbf{k}$.

to multiply the following matrix for the transformation from (k_x^L, k_y^L, k_z^L) to (k_x^r, k_y^r, k_z^r):

$$\begin{pmatrix} 1 & 0 & 0 \\ 0 & \cos\alpha & -\sin\alpha \\ 0 & \sin\alpha & \cos\alpha \end{pmatrix} \begin{pmatrix} \cos\beta & -\sin\beta & 0 \\ \sin\beta & \cos\beta & 0 \\ 0 & 0 & 1 \end{pmatrix} \tag{3.16}$$

Let θ and ϕ be the polar and azimuthal angles of $\mathbf{k}'$ with respect to the initial wave vector $\mathbf{k}$, as shown in Figure 3.8. Then the k_x, k_y, and k_z components in the (k_x^r, k_y^r, k_z^r) frame are given by

$$(k' \sin\theta \cos\phi,\ k' \sin\theta \sin\phi,\ k' \cos\theta) \tag{3.17}$$

Therefore, vector $\mathbf{k}'$ in the (k_x^L, k_y^L, k_z^L) frame is given by multiplying the inverse matrix of (3.16); thus,

$$\begin{pmatrix} \cos\beta & \cos\alpha \sin\beta & \sin\alpha \sin\beta \\ -\sin\beta & \cos\alpha \cos\beta & \sin\alpha \cos\beta \\ 0 & -\sin\alpha & \cos\alpha \end{pmatrix} \tag{3.18}$$

where sines and cosines in the matrix elements of (3.18) are given as

$$\sin\alpha = \frac{\sqrt{k_x^2 + k_y^2}}{k}, \qquad \cos\alpha = \frac{k_z}{k}$$
$$\sin\beta = \frac{k_x}{\sqrt{k_x^2 + k_y^2}}, \qquad \cos\beta = \frac{k_y}{\sqrt{k_x^2 + k_y^2}} \tag{3.19}$$

Combining (3.17), (3.18), and (3.19), the components of the wave vector after scattering in terms of the (k_x^L, k_y^L, k_z^L) frame are obtained as

$$\begin{pmatrix} k_x' \\ k_y' \\ k_z' \end{pmatrix} = \begin{pmatrix} \dfrac{k_y}{\sqrt{k_x^2 + k_y^2}} & \dfrac{k_x k_z}{k\sqrt{k_x^2 + k_y^2}} & \dfrac{k_x}{k} \\ \dfrac{-k_x}{\sqrt{k_x^2 + k_y^2}} & \dfrac{k_y k_z}{k\sqrt{k_x^2 + k_y^2}} & \dfrac{k_y}{k} \\ 0 & \dfrac{-\sqrt{k_x^2 + k_y^2}}{k} & \dfrac{k_z}{k} \end{pmatrix} \begin{pmatrix} k' \sin\theta \cos\phi \\ k' \sin\theta \sin\phi \\ k' \cos\theta \end{pmatrix} \tag{3.20}$$

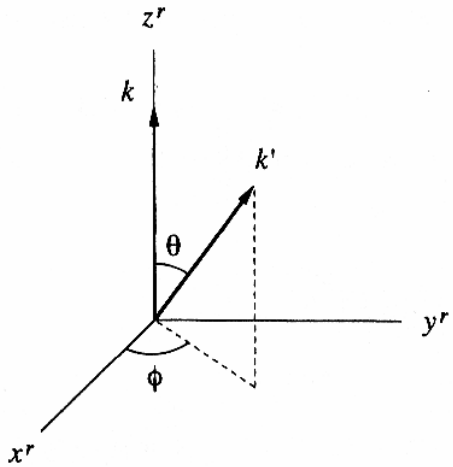

Figure 3.8 Definition of the polar angle θ and the azimuthal angle ϕ of $\mathbf{k}'$ with respect to the initial wave vector $\mathbf{k}$.

In case of isotropic scattering in ellipsoidal bands, the final wave vector in terms of the laboratory frame can be obtained by making use of the Herring-Vogt transformation (see Chapter 2):

$$\mathbf{k}^* = U\mathbf{k} \tag{3.21}$$

which transforms the ellipsoidal surfaces to the spherical surfaces, where U is given by (2.139). The carrier energy in terms of $\mathbf{k}^*$ can then be written as

$$E_{\mathbf{k}} = \frac{\hbar^2}{2}\left(\frac{k_x^2}{m_x^*} + \frac{k_y^2}{m_y^*} + \frac{k_z^2}{m_z^*}\right) = \frac{(\hbar k^*)^2}{2m_f} \tag{3.22}$$

The procedure to evaluate the components (k_x^L, k_y^L, k_z^L) is summarized as follows. First we evaluate k'^* from $E_{\mathbf{k}}'$ using (3.22); thus, $k'^* = \sqrt{2m_f E_{\mathbf{k}'}}/\hbar$. Then we evaluate the components $(k_x'^*, k_y'^*, k_z'^*)$ on the spherical surface using (3.11) and (3.12). Finally, (k_x^L, k_y^L, k_z^L) can be obtained by multiplying $(k_x'^*, k_y'^*, k_z'^*)$ by the inverse of U.

The full three-dimensional representation (k_x, k_y, k_z) may not be necessary

for the carrier transport analysis in a bulk semiconductor; however, this representation is adopted in this book because the subroutines developed for the single-particle Monte Carlo program can also be used for the device analysis after minor revisions are made.

Figure 3.9 shows the remaining half of the subroutine **scat** in which the

```
c
c---( Determination of final states )---
c
   20 kf  = smh(iv)*sqrt(ef)
      f   = 2.*ki*kf/(ki-kf)/(ki-kf)
      if (f.le.0.) return
      cb  = (1.+f-(1.+2.*f)**rnd())/f
c
   30 sb  = sqrt(1.-cb*cb)
      fai = 2.*pi*rnd()
      cf  = cos(fai)
      sf  = sin(fai)
      skk = sqrt(skx+sky)
      a11 = ky/skk
      a12 = kx*kz/skk/ki
      a13 = kx/ki
      a21 =-kx/skk
      a22 = ky*kz/skk/ki
      a23 = ky/ki
      a32 =-skk/ki
      a33 = kz/ki
      x1  = kf*sb*cf
      x2  = kf*sb*sf
      x3  = kf*cb
      kx  = a11*x1+a12*x2+a13*x3
      ky  = a21*x1+a22*x2+a23*x3
      kz  =        a32*x2+a33*x3
      return
```

Figure 3.9 Remaining half of FORTRAN code for the subroutine **scat**.

```
c
   40 kf  = smh(iv)*sqrt(ef)
      cs  = 1.-2.*rnd()
      sn  = sqrt(1.-cs*cs)
      fai = 2.*pi*rnd()
      kx  = kf*cs
      ky  = kf*sn*cos(fai)
      kz  = kf*sn*sin(fai)
      return
      end
```

Figure 3.9 Continued

determination of the wave vector after scattering is made. The phonon scattering (polar optical phonon and acoustic phonon) and impurity scattering are included in the program. The list shown in Figure 3.9 can be combined with the one shown in Figure 3.6 to complete the subroutine **scat**.

At this point, we now have all the information necessary for writing a program for the single-particle Monte Carlo calculation except that of the physical constants and material parameters. These must be specified for the material under investigation and included in a separate subroutine. An example of a complete single particle Monte Carlo program used for the calculation of the mean electron velocity in bulk GaAs is found in Appendix 6.1.

3.1.4 Velocity Calculation

Having outlined in the previous sections the single particle Monte Carlo method, we next apply this method to the calculation of the mean carrier velocity in a bulk semiconductor under the application of a uniform bias electric field. We first describe the method used to calculate the mean carrier velocity and energy, and present the simulation results later on.

The Monte Carlo method described is equivalent to solving the Boltzmann transport equation. Therefore, if we accumulate the flight time (or visiting time) of an electron in each volume element of k-space, we are able to figure out the distribution function by which the mean carrier velocity and energy can be calculated. This procedure requires a large amount of memory to accumulate the data in k-space. However, it is not necessary to do this, because the mean values of velocity and energy can be calculated directly by monitoring each electron flight and then taking an average over all flights.

The instantaneous carrier velocity is given by

$$\mathbf{v} = \frac{1}{\hbar}\nabla_{\mathbf{k}} E_{\mathbf{k}} \tag{3.23}$$

Therefore, the mean carrier velocity during flight time τ can be written as

$$\langle \mathbf{v} \rangle_\tau = \frac{1}{\hbar}\frac{\Delta E_{\mathbf{k}}}{\Delta \mathbf{k}} \tag{3.24}$$

where $\Delta E_{\mathbf{k}}$ and $\Delta \mathbf{k}$ are small increments of the carrier energy and wave vector during τ, respectively. According to (3.8), the increment of electron wave vector under a constant electric field is given by

$$\Delta \mathbf{k} = -\frac{e\mathbf{F}}{\hbar}\tau \tag{3.25}$$

Substituting (3.25) into (3.24), we have

$$\langle \mathbf{v} \rangle_\tau = -\frac{\Delta E_{\mathbf{k}}}{e\mathbf{F}\tau} \tag{3.26}$$

Making use of the mean carrier velocity during τ given by (3.26), the mean carrier velocity during the total simulation time T is obtained as

$$\begin{aligned} \langle \mathbf{v} \rangle_T &= \frac{1}{T}\sum \langle \mathbf{v} \rangle_\tau \tau \\ &= -\frac{1}{e\mathbf{F}T}\sum \Delta E_{\mathbf{k}} \\ &= -\frac{1}{e\mathbf{F}T}\sum (E_f - E_i) \end{aligned} \tag{3.27}$$

where E_i is the carrier energy at the start of the electron flight and E_f is the energy at the end of the flight. The summation has to be made for all free flights. Equation (3.27) shows that we need to accumulate the energy increment during each free flight. The same reasoning leads to mean carrier energy $\langle E \rangle_T$ being derived as

$$\langle E \rangle_T = \frac{1}{T} \sum \langle E \rangle_\tau \tau \tag{3.28}$$

where $\langle E \rangle_\tau$ is given to a good approximation by

$$\langle E \rangle_\tau = \frac{E_i + E_f}{2} \tag{3.29}$$

To evaluate $\langle \mathbf{v} \rangle_T$ and $\langle E \rangle_T$, the calculation of $\langle \mathbf{v} \rangle_\tau$ and $\langle E \rangle_\tau$ must be added to the subroutine **drift**.

Figure 3.10 shows a new subroutine **drift1**, in which there is the accumulation of data for the mean velocity and energy. To save computing time, E_i is transferred from **scat** as the carrier energy at the start of the electron flight and E_f is transferred back to **scat** as the initial energy before scattering via the common block */com1/*. The subroutine **scat** has to be modified to be consistent with the new subroutine **drift1**. However, this may be a simple exercise for the reader.

Based on the method explained above, the carrier velocity versus electric field curves ($\mathbf{v}$-*F curves*) for bulk silicon and GaAs are calculated. The various parameters related to the scattering processes considered in these simulations are summarized in Appendix 1.

Figure 3.11 shows the $\mathbf{v}$-F curves calculated for electrons in bulk silicon at the lattice temperatures of 77K and 300K. The carrier concentration is assumed to be 1×10^{14} cm^{-3}. The electric field is varied from 0.1 to 300 kV/cm and the orientation of the electric field is chosen to be parallel to the ⟨100⟩ direction. The anisotropy and non-parabolicity of the X-valleys are taken into account. The scattering mechanisms taken into account are acoustic phonon scattering, non-polar optical phonon scattering, and impurity scattering. It can be seen in Figure 3.11 that the $\mathbf{v}$-F curves calculated are almost consistent with the measured data [4].

Figure 3.12 shows the low-field electron mobility calculated for bulk silicon with various impurity concentrations. The impurity concentration varies from 1×10^{14} to 5×10^{18} cm^{-3}. The low-field mobilities calculated are almost consistent with the measured data [5] when the impurity concentration is relatively low (below 10^{17} cm^{-3}). However, the mobility calculated is much higher than that measured when the impurity concentration is above 10^{17} cm^{-3}. This may be due to the rather simplified calculation of the impurity scattering, which is based on the Born approximation. At high impurity concentrations, more sophisticated models are needed, in which a complicated many-body process can be taken into account [6].

Figure 3.13 shows the low-field electron mobility in silicon at various lattice temperatures; the lattice temperature varies from 40K to 400K. The impurity scattering is not taken into account to see clearly the temperature dependence of the


```
c
c===( Calculation of drift process )===
c
      subroutine drift1(tau)
      common
     &/com1/kx,ky,kz,sk,e,iv
     &/dri/qh
     &/field/fx
     &/ek/smh(2),hhm(2),ec(2)
     &/ave/av,ae
      real kx,ky,kz
c
      ei  = e
c
      dkx = qh*fx*tau
      kx  = kx+dkx
c
      sk  = kx*kx+ky*ky+kz*kz
      ef  = hhm(iv)*sk
      av  = av + (ef-ei)
      ae  = ae + (ef+ei+ec(iv))*tau
c
      e   = ef
c
      return
      end
```

Figure 3.10 FORTRAN code for the subroutine **drift1**.

mobility on the phonon scattering. It can be seen in Figure 3.13 that the temperature dependence of the mobility is nearly proportional to $T^{-3/2}$ when the lattice temperature is roughly below 100K. This is consistent with the fact that the characteristic exponent of the mobility solely determined by the acoustic phonon is $-3/2$.

Figure 3.14 shows the $\mathbf{v}$-F curves for electrons in bulk GaAs at the lattice temperature of 300K. A two-valley model was employed here in which only the Γ-valley and L-valleys are taken into account. Furthermore, it is assumed that both

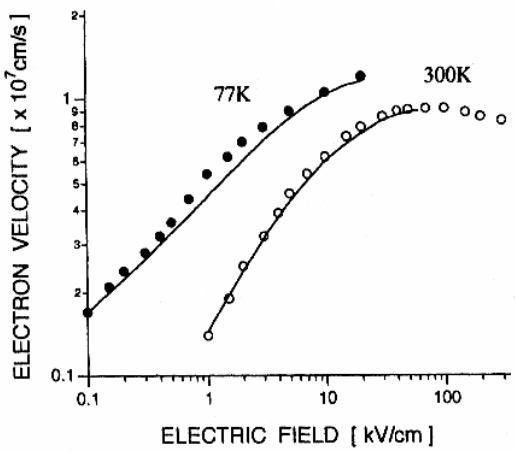

Figure 3.11 Electron velocity versus electric field characteristics calculated for bulk silicon at 77K and 300K. The solid lines show the experimental data [4].

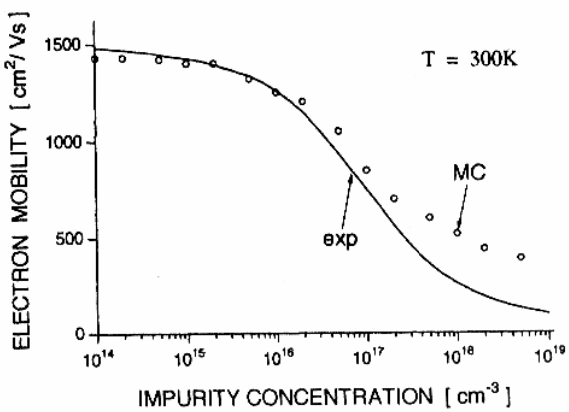

Figure 3.12 Low-field electron mobility calculated for bulk silicon with various impurity concentrations. The lattice temperature is assumed to be 300K. The solid line shows the measured data [4].

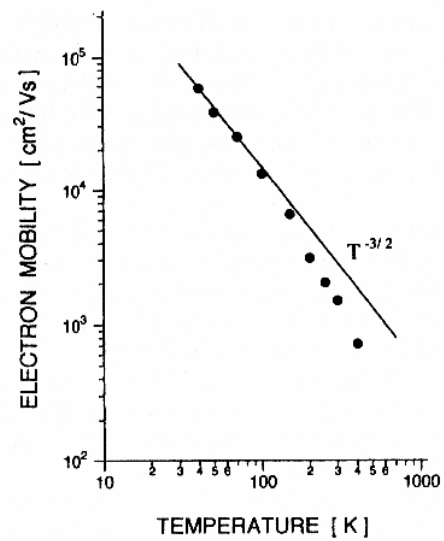

Figure 3.13 Low-field electron mobility calculated for bulk silicon at various lattice temperatures. The impurity scattering is not taken into account. The solid line shows the slope of $-3/2$.

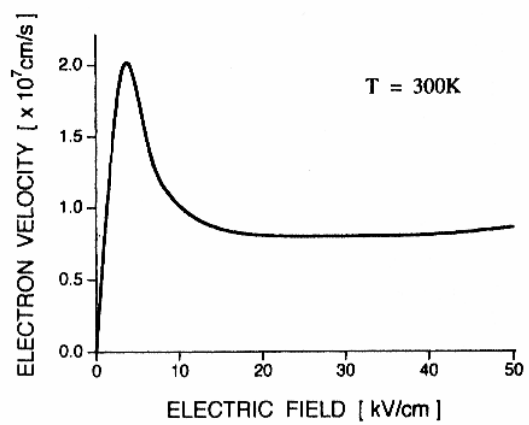

Figure 3.14 Electron velocity versus electric field characteristics calculated for bulk GaAs at 300K. The impurity concentration is assumed to be 1×10^{14} cm^{-3}.

Γ-valley and L-valleys are non-parabolic. However, the anisotropy of the L-valleys is not taken into account, and thus the L-valleys are modeled as four equivalent spherical bands, where the density-of-states effective mass m_d^* is employed for the scattering calculation. The scattering mechanisms taken into account are the intravalley (acoustic and polar optical) and intervalley (non-polar optical) phonon scatterings and the ionized impurity scattering. The program used can be found in Appendix 6.

Figure 3.14 shows that the $\mathbf{v}$-F curves typically present a decrease of the electron velocity when the electric field is increased above the threshold value (about 4 kV/cm); this effect is known as the *negative differential conductivity* (NDC). The NDC is due to the transfer of electrons from the Γ-valley, where they have small effective mass, to the L-valleys, where they have a larger effective mass, and has been predicted by Ridley, Watkins, and Hilsum (see also Chapter 11 of [5]).

Figure 3.15 shows the mean electron energy versus electric field curve for bulk GaAs at 300K. It can be seen that the mean electron energy increases steeply with the increase of the electric field until it reaches about 0.2 eV. Beyond this point, the energy increases only slowly with a further increase of the electric field. This feature is due to the electron transfer from the Γ-valley to the L-valleys and is related to the energy relaxation rate due to the non-polar optical phonon scattering in the L-valleys, which is much larger than that due to the polar optical phonon scattering in the Γ-valley.

The electron transfer from the Γ-valley to the L-valleys is clearly observed if we plot the electron occupancy in each valley, as shown in Figure 3.16. It can be

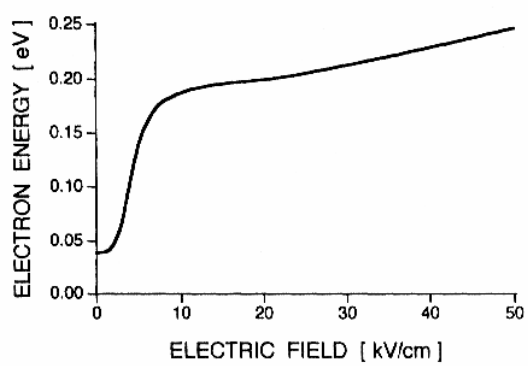

Figure 3.15 Mean electron energy versus electric field curve calculated for bulk GaAs at 300K. The impurity concentration is assumed to be 1×10^{14} cm^{-3}.

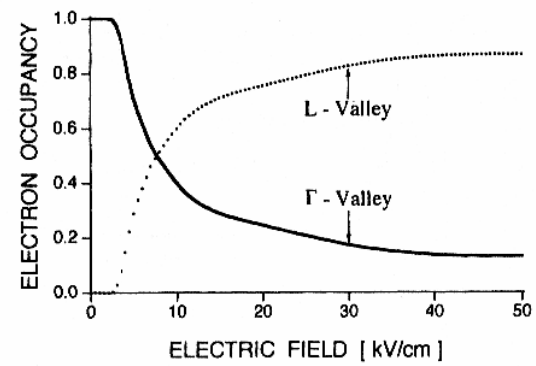

Figure 3.16 Electron occupancy in the Γ- and L-valleys calculated for bulk GaAs at 300K. The impurity concentration is assumed to be 1×10^{14} cm^{-3}.

seen that the electron population in the Γ-valley decreases with the increase of the electric field, while that in the L-valleys increases. Figure 3.16 also shows that population inversion is observed at electric fields of about 8 kV/cm. If we compare the electron occupancy with the mean electron energy shown in Figure 3.15, we see in fact that the electron transfer is mostly completed when the mean electron energy reaches roughly the value of the Γ-L energy separation.

Figure 3.17 shows the $\mathbf{v}$-F curves of electrons in bulk GaAs with impurity concentrations of 1×10^{14} cm^{-3} and 1×10^{17} cm^{-3}. It can be seen that both the low-field mobility (the slope of the curves at low field) and the electron peak velocity (observed around 4 kV/cm) decrease with the increase of the impurity concentration. Because of the decrease of these values, it is expected that the NDC may disappear when the impurity concentration exceeds a certain value.

3.2 ENSEMBLE MONTE CARLO FOR BULK ELECTRONS

As discussed in the previous section, the single particle Monte Carlo method is a useful tool for the calculation of carrier transport, especially in the case of steady-state carrier transport under a static and uniform electric field. An ensemble Monte Carlo method can, however, be used more widely for many other purposes, such as the analysis of carrier diffusion, the carrier transport in an inhomogeneous field, the non-stationary behavior of carriers, and so on. We describe the details of such an ensemble Monte Carlo method as applied to carrier transport in a bulk crystal.

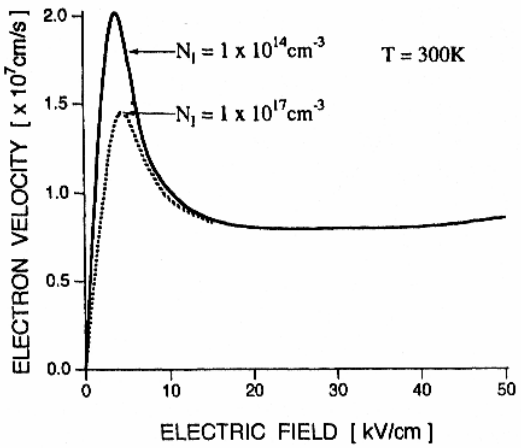

Figure 3.17 Electron velocity versus electric field characteristics calculated for bulk GaAs with impurity concentrations of 1×10^{14} cm^{-3} and 1×10^{17} cm^{-3}.

3.2.1 Ensemble Particle Motion

The ensemble Monte Carlo method is based on the successive and simultaneous calculation of the motions of many particles during a small time increment Δt. The method is essentially dynamic, and is therefore suitable for the analysis of transient carrier motions. However, it can also be applied to stationary problems by continuing the calculations until the system reaches a steady state.

Figure 3.18 shows schematically the flowchart of an ensemble Monte Carlo calculation. The horizontal lines show the trajectories of particles on the time coordinate. The time increases to the right of each line. The vertical broken lines show the time when the many-particle system is observed. The interval between two adjacent broken lines corresponds to the time increment Δt between two observations. Each **x** on the horizontal lines shows the time at which scattering occurs. Hence, the interval between two adjacent **x**'s is the free-flight time. For the observation of the whole particle system, the particle positions in real space and momentum space must be calculated every Δt. Even if the applied electric field is stationary, Δt should be chosen small enough so that the scattering rates can be updated with the change of the electron energy with time.

The ensemble Monte Carlo method can be carried out by preparing a subroutine **emc** in which a couple of subroutines for the drift and scattering processes are employed. The subroutines **drift** and **scat** developed for the single-particle Monte Carlo method can also be used for the ensemble Monte Carlo method after

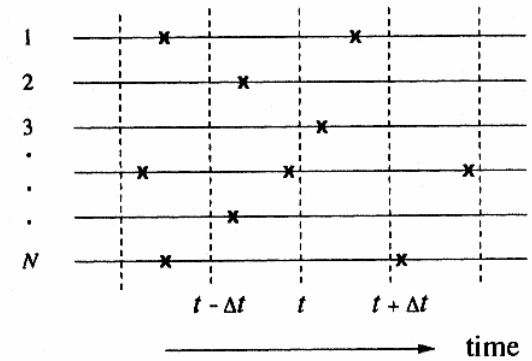

Figure 3.18 Flowchart of ensemble Monte Carlo simulation. Each horizontal solid line shows the trace of each particle. The vertical broken line shows sampling time. The **x** on the solid line shows the scattering time.

making minor revisions. The new subroutine **emc** used for the ensemble Monte Carlo calculations is different from the subroutine **smc** shown in Figure 3.2. The main difference arises from the fact that the ensemble Monte Carlo calculation is carried out by repeating the drift and scattering calculations during Δt for all particles.

If we pay attention to the motion of a particle during the interval Δt (say, between t and $t + \Delta t$), we notice that scattering events take place randomly. We cannot therefore tell the number of times that the particle will be scattered during Δt. To simulate such a motion from t to $t + \Delta t$, let us assume that the position and momentum vectors are known at t and assume that the first scattering time t_S after t can be determined by a random number. If t_S is larger than $t + \Delta t$, then the particle merely drifts during Δt. If t_S is less than $t + \Delta t$, the particle is scattered before $t + \Delta t$. In this case, the particle drifts first during $(t_S - t)$ and is scattered at t_S. The new scattering time t_S has then to be determined by another random number. Following this, we check again whether the new t_S is larger than $t + \Delta t$ or not and continue to do so until the end of the simulation. A flowchart of the subroutine **emc** for the ensemble Monte Carlo calculation based on the above consideration is shown in Figure 3.19.

The corresponding FORTRAN code for the subroutine **emc** is shown in Figure 3.20. The parameters used in the subroutine **emc** are described in Table 3.4. As seen in the list of the subroutine, the position and wave vectors of all the particles are kept on record during the simulation. Therefore, the common block */com1/* for the subroutines **drift** and **scat** must be modified to be consistent with that of the subroutine **emc**.

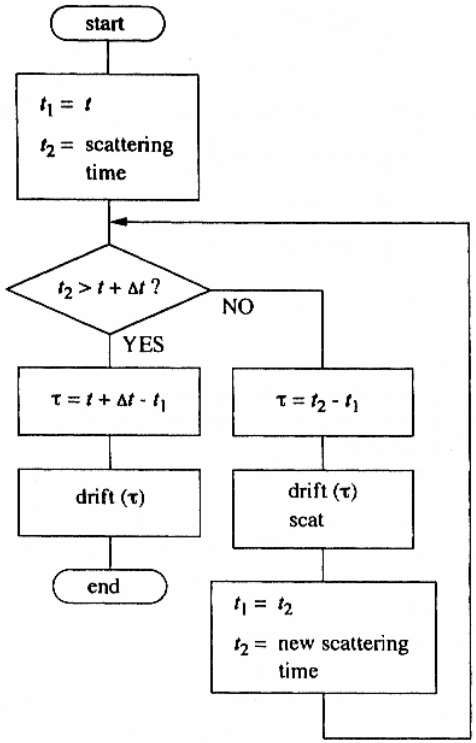

Figure 3.19 Flowchart of the subroutine **emc**.

The increment of the position vector $\Delta\mathbf{r}$ during flight time τ can be calculated according to the equations of motion. If the electric field $\mathbf{F}$ during Δt is assumed to be constant, $\Delta\mathbf{r}$ can be expressed by the average carrier velocity during the flight time multiplied by the flight time, and thus we have

$$\Delta\mathbf{r} = \langle\mathbf{v}\rangle_\tau \tau \tag{3.30}$$

where $\langle\mathbf{v}\rangle_\tau$ is given by (3.26). The calculation of $\Delta\mathbf{r}$ must be added to the subroutine **drift** if the particle positions are required. Figure 3.21 shows a FORTRAN code of a new subroutine **drift2** which can be used for the ensemble Monte Carlo method.


```
c
c===( Particle motion during dt )===
c
      subroutine emc
      common
     &/com1/kx,ky,kz,ts,x,y,iv
     &/com2/pt(10000,6),ipt(10000)
     &/gamma/gm
     &/num/inum
     &/time/dt,t
      real kx,ky,kz
c
      tdt = t + dt
      do 30 n = 1,inum
         kx = pt(n,1)
         ky = pt(n,2)
         kz = pt(n,3)
         ts = pt(n,4)
         x  = pt(n,5)
         y  = pt(n,6)
         iv = ipt(n)
```

Figure 3.20 FORTRAN code for the subroutine **emc**.

3.2.2 Velocity Overshoot

There has been considerable interest in the electron transport in submicron devices for possible high-frequency and high-speed applications. As the transit time of electrons in a device becomes comparable to, or less than, the relaxation time of electrons, cold electrons injected into the device may not reach their steady-state velocity during their transit through the device. It is therefore important to realize that the velocity-field curves calculated in the previous section may not be applicable to the transport of electrons in submicron-sized devices. The transient nature after injection allows the mean velocity to overshoot the usual saturation value. This phenomenon has been extensively studied with the ensemble Monte Carlo method [7].

This section shows some results of the ensemble Monte Carlo simulations for the transient electron transport in bulk silicon and GaAs. The background doping

```
c
          t1 = t
   10     if (ts.gt.tdt) go to 20
          tau = ts - t1
          call drift2(tau)
          call scat
          t1  = ts
          ts  = t1 - alog(rnd())/gm
          go to 10
   20     tau = tdt - t1
          call drift2(tau)
c
          pt(n,1) = kx
          pt(n,2) = ky
          pt(n,3) = kz
          pt(n,4) = ts
          pt(n,5) = x
          pt(n,6) = y
          ipt(n)  = iv
   30 continue
      return
      end
```

Figure 3.20 Continued

concentration is assumed to be 10^{14} cm^{-3} for both materials. The various material parameters related to electron scattering are the same as those used for the single-particle Monte Carlo calculation shown in Section 3.1 and are summarized in Appendix 1. It is assumed that a uniform electric field is applied throughout the bulk crystal. The applied electric fields are 2, 5, 10, 20, and 50 kV/cm. Figures 3.22 and 3.23 show the time evolution of the mean drift velocity of the electrons injected cold at a position ($x = 0$) we call the cathode, and drifting in a region of uniform electric field. We note that for both silicon and GaAs, the velocities exhibit large transient overshoots at high fields before the steady state values are reached. This is due to the disparity of the momentum and energy relaxation times as functions of electron energy. Transient overshoot is typically observed when the electric field applied is so high that electrons can reach the high-energy region, where the momentum relaxation time is smaller than the energy relaxation time.

Table 3.4
Parameters Used in the Subroutine emc

Parameter	*Description*
kx, ky, kz	Components of wave vector
ts	Scattering time
x, y	x and y components of position vector
iv	Valley index $\begin{cases} \text{iv} = 1 \text{ for } \Gamma\text{-valley} \\ \text{iv} = 2 \text{ for } L\text{-valley} \end{cases}$
pt(10000,6)	Dimension storing particle data
ipt(10000)	Dimension storing valley indices
gm	Total scattering rate, Γ
inum	Number of particle
dt	Time increment
t	Time
tau	Flight time

shifted in momentum space. Somewhat later, energy relaxation becomes effective so that the distribution function spreads and the drift velocity decreases.

We also note that the velocity overshoot in GaAs is only observed when the electric field is higher than about 3 kV/cm, above which strong non-equivalent intervalley phonon scatterings between the Γ- and L-valleys take place; hence, the momentum relaxation time becomes small.

Figures 3.24 and 3.25 show the drift velocity as a function of distance from the source; a presentation of this kind is more relevant to the discussion of electron transport in submicron semiconductor devices. The distance over which the drift velocity overshoots the saturation value in silicon is much smaller than that in GaAs. Since the range of velocity overshoot in silicon is less than 0.1 μm, the speed performance of silicon devices with dimensions larger than 0.1 μm may not be affected by the overshoot phenomenon. Electrons in GaAs can, however, travel at a velocity above their steady-state value for a distance of nearly 1 μm. GaAs devices of submicron dimensions may therefore be substantially affected by velocity overshoot effects.

3.3 SUMMARY

The single-particle and ensemble Monte Carlo methods have been described in this chapter. Flowcharts and appropriate FORTRAN codes were provided so that readers could develop their own programs.

Basic carrier transport mechanisms in silicon and GaAs are studied with the help of the programs presented in this book. The calculated transport properties

```
c
c===( Calculation of drift process for EMC )===
c
      subroutine drift2(tau)
      common
     &/com1/kx,ky,kz,ts,x,y,iv
     &/dri/qh
     &/field/fx
     &/nonp/af(2),af2(2),af4(2)
     &/ek/smh(2),hhm(2),ec(2)
     &/hm2/hm(2)
      real kx,ky,kz
c
      dkx = qh*fx*tau
c
      cp  = hm(iv)*tau
      sk  = kx*kx+ky*ky+kz*kz
      gk  = hhm(iv)*sk
      sq  = sqrt(1.+af4(iv)*gk)
c
      x   = x+cp*(kx+0.5*dkx)/sq
      y   = y+cp*ky
c
      kx = kx+dkx
c
      return
      end
```

Figure 3.21 FORTRAN code for the subroutine **drift2**.

in some cases may differ from experimental characteristics due to uncertainty in knowing the precise values of various material parameters. However, the reader can find some transport phenomena typically observed in sub-micrometer region, which are termed velocity overshoot or non-stationary transport. The readers are encouraged to develop their own programs based on the programs presented in this chapter and in Appendix 6 and are encouraged to observe the phenomena for themselves.

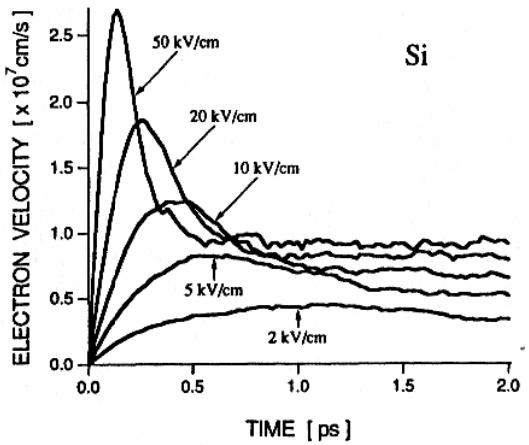

Figure 3.22 Time evolution of the mean drift velocity of electrons in bulk silicon.

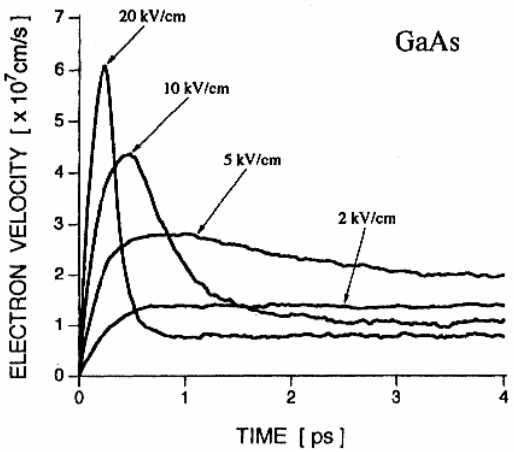

Figure 3.23 Time evolution of the mean drift velocity of electrons in bulk GaAs.

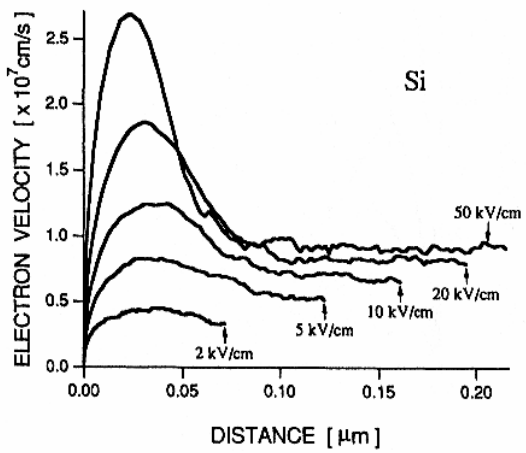

Figure 3.24 Drift velocity overshoot as a function of distance in bulk silicon.

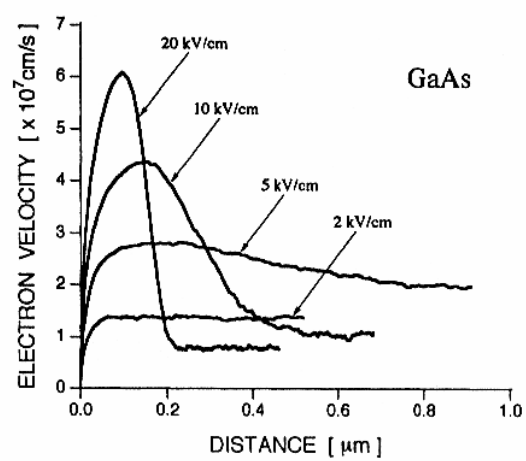

Figure 3.25 Drift velocity overshoot as a function of distance in bulk GaAs.

3.4 TO PROBE FURTHER

The Monte Carlo calculations demonstrated in this chapter are limited to electron transport in bulk GaAs and silicon. However, many simulations of the carrier transport in bulk semiconductors have been presented after the pioneering work by Kurosawa [1]. Since the aim of this book is not to provide a review of the development of the Monte Carlo Method, we only introduce some useful papers and books for further study.

A systematic study of electron transport in bulk GaAs has been done by Fawcett et al. [2]. An excellent review of its development is made by Jacoboni and Reggiani [3]. The book by Jacoboni and Lugli covers many topics and references [8]. Nice introductory reports for Monte Carlo method are presented by Price [9] and Boardman [10]. There may be some readers who are interested in very-high-field transport and feel that the effective mass approximation may not be adequate even though the non-parabolic factor is taken into account. These readers should read the paper by Fischetti and Laux [11], in which Monte Carlo modeling beyond the effective mass approximation, using the band structure obtained from the empirical pseudopotential method, is presented.

The reader who is interested in the numerical method for generating pseudorandom numbers should see the book by Press et al. [12].

PROBLEMS

[3.1] Derive (3.5).

[3.2] Write a program to generate 1000 free-flight times using (3.5) and then calculate the average flight time. Assume $\Gamma = 1 \times 10^{14}$ [s^{-1}].

[3.3] Derive (3.11), by which the azimuthal angle ϕ' and polar angle θ' for isotropic scattering is determined.

[3.4] Modify the subroutine **scat** shown in Figure 3.6 for the carrier transport in non-parabolic bands. *Hint*: The electron energy before scattering and the electron wave vector after scattering must be calculated by the non-parabolic *E-k* relation.

[3.5] Modify the subroutine **drift1** shown in Figure 3.10 for the carrier transport in non-parabolic bands.

[3.6] Based on the program shown in Sections 6.1 and 6.2 of Appendix 6, develop a single-particle Monte Carlo program for the transport of electrons in bulk silicon, in which the non-parabolicity and anisotropy of the conduction bands are taken into account.

[3.7] Based on the program shown in Section 6.3 of Appendix 6, develop an ensemble Monte Carlo program for carrier diffusion in bulk GaAs.

REFERENCES

[1] Kurosawa, K., "Monte Carlo Calculation of Hot Electron Problems," *Journal of the Physical Society of Japan*, Vol. 21, Supplement, 1966, pp. 424–426.

[2] Fawcett, W., A. D. Boardman, and S. Swain, "Monte Carlo Determination of Electron Transport in Gallium Arsenide," *Journal of the Physics and Chemistry of Solids*, Vol. 31, 1970, pp. 1962–1990.

[3] Jacoboni, C., and L. Reggiani, "The Monte Carlo Method for the Solution of Charge Transport in Semiconductors With Application to Covalent Material," *Review of Modern Physics*, Vol. 55, 1983, pp. 645–705.

[4] Jacoboni, C., C. Canali, G. Ottaviani, and A. A. Quaranta, "A Review of Some Charge Transport Properties of Silicon," *Solid-State Electronics*, Vol. 20, 1977, pp. 77–89.

[5] Sze, S. M., *Physics of Semiconductor Devices*, New York: John Wiley, 1981.

[6] Ridley, B. K., *Quantum Processes in Semiconductors*, London: Oxford, 1982.

[7] Ruch, J. G., "Electron Dynamics in Short Channel Field-Effect Transistors," *IEEE Transaction on Electronic Devices*, Vol. ED-19, 1972, pp. 652–654.

[8] Jacoboni, C., and P. Lugli, *The Monte Carlo Method for Semiconductor Device Simulation*, Wien: Springer-Verlag, 1989.

[9] Price, P. J., "Monte Carlo Calculation of Electron Transport in Solids," *Semiconductors and Semimetals*, Vol. 14, 1979, pp. 249–334.

[10] Boardman, A. D., ed., "Computer Simulation of Hot Electron Behaviour in Semiconductors Using Monte Carlo Methods," Chapter 11 in *Physics Programs*, New York: John Wiley, 1980.

[11] Fischetti, M. V., and S. E. Laux, "Monte Carlo Analysis of Electron Transport in Small Semiconductor Devices Including Band-Structure and Space-Charge Effects," *Physical Review B*, Vol. 38, No. 14, 1988, pp. 9721–9745.

[12] Press, W. H., B. P. Flannery, S. A. Teukolsky, and W. T. Vetterling, *Numerical Recipes*, Cambridge, New York: Cambridge University Press, 1987.

Chapter 4
Monte Carlo Device Simulation

4.1 INTRODUCTION

Having introduced the details of the Monte Carlo method for carrier transport in bulk semiconductors in Chapter 3, we are now ready to discuss the application of the Monte Carlo method to the analysis of semiconductor devices.

In the ensemble Monte Carlo method for device simulation, two things have to be taken into account in addition to the ensemble Monte Carlo method for bulk semiconductors. One is that the motion of particles is spatially restricted in a device model, contrary to the case in a bulk semiconductor, in which the motion spreads in a boundless region. Hence, we need to set up suitable boundary conditions for particles that reach the surface of the device model. During the simulation, particles may be *reflected* at the surface of the device model or may *exit* or *enter* the area of the device model through the terminals. The other thing to be taken into account is that the potential calculation must be done self-consistently with the distribution of particles through the solution of the Poisson equation with appropriate boundary conditions. The boundary conditions applied to the carrier dynamics must be consistent with those applied to the Poisson equation. Hence, we need the following arrangements in the Monte Carlo device simulations:

1. Calculation of particle dynamics with appropriate boundary conditions;
2. Handling of particles associated with the exit or entrance of particles through the terminals of the device model;
3. Self-consistent potential calculation with appropriate boundary conditions.

Topics related to 1 and 2 are discussed in Section 4.2, while point 3 is treated in Section 4.3.